scientific reports

Check for updates

OPEN

Fast photo-carrier multiplication by engineered potential trap in MoS_2/Ge double junction phototransistor

Youngseo Park[1], Minhyeok Jung[2], Han Beom Jeong[3], Hu Young Jeong[4], Sangwan Sim[5], Geonwook Yoo[6] & Junseok Heo[1,2]✉

Broadband photodetectors in the visible and short-wave infrared wavelengths have garnered significant interest in recent years as a desirable method to achieve better detection in adverse weather conditions. Many material combinations have been proposed to replace expensive III-V based photodetectors; however, the photodetection performance of these novel material and device concepts showed undesirable performances due to uncontrollable charge-trap-based photomultiplication, preventing fast photoresponse and gain. To solve this issue, we devised an engineered potential trap in Ge/MoS_2 double junction phototransistor which show a high responsivity of 7.6 A/W (corresponding to an external quantum efficiency of 2,024%) as well as a fast photoresponse of 88.1 µs. The maximum photocurrent gain reaches 29.1 with broadband imaging capability. This excellent performance is achieved through photogenerated hole confined in p-Ge clad by MoS_2 and n-Ge induced multiple electrons, which diminished rapidly via recombination upon removal of illumination. Our device concept enables creation of highly sensitive fast broadband imaging based on mixed dimensional van der Waals heterojunctions.

Keywords Photocurrent multiplication, Potential trap, Broadband photodetector, SWIR, Van der waals, Germanium, MoS_2

The photodetection and visualization of short-wave infrared (SWIR) light ranging from 1 to 3 µm has garnered significant interest owing to the unprecedented advantages of high visibility in adverse weather and at night[1–5]. The lower Rayleigh scattering compared with the scattering of visible light owing to a longer wavelength allows a clear vision of haze. The SWIR light from nightglow facilitates night vision, including during dark moons. Hence, SWIR photodetection has been extensively utilized in various applications such as medical diagnostics[4,6–8], semiconductor inspection[3,4], astronomy[3], face recognition[9], and automotive[5]. Furthermore, broadband photodetection, which senses both visible and SWIR lights, is critical for compensating SWIR imaging. In automotives, for example, it is beneficial to render a color on SWIR imaging to identify traffic lights or road conditions[3].

To date, commercially available InGaAs photodiodes epitaxially grown on InP substrates have been predominantly employed for SWIR photodetection. However, the high material costs and limited responsivities of InGaAs photodiodes without carrier multiplications restrict their widespread usage in consumer products. Hence, various emerging materials such as graphene[10,11], quantum dots (QDs)[10–12], and black phosphorus[13,14] have been proposed for implementing highly responsive SWIR photodetectors in diverse device structures such as PN diodes[14,15], Schottky junction diodes[16], and field effect transistors (FETs)[11–13,17]. Furthermore, broadband photodetection has been demonstrated by adjoining a material with another material of a larger bandgap[18,19]. However, previous studies have relied on unintentionally present charge traps to obtain a photocurrent gain. A strong confinement of photogenerated carriers in the traps may result in a high responsivity; however, a slow response time is imminent owing to the uncontrollable delayed release of trapped charges. Ni et al. reported an ultrahigh responsivity of 10^9 A/W at a wavelength of 1450 nm in a Si QDs/graphene FET; however, its slow

[1]Department of Electrical and Computer Engineering, Ajou University, Suwon 16499, South Korea. [2]Department of Intelligence Semiconductor Engineering, Ajou University, Suwon 16499, South Korea. [3]Department of Materials Science and Engineering, Korea Advanced Institute of Science and Technology (KAIST), Daejeon 34141, South Korea. [4]Graduate School of Semiconductor Materials and Devices Engineering, Ulsan National Institute of Science and Technology (UNIST), Ulsan 44919, South Korea. [5]Division of Electrical Engineering, Hanyang University, Ansan 15588, South Korea. [6]School of Electronic Engineering, Soongsil University, Seoul 06938, South Korea. ✉email: jsheo@ajou.ac.kr

response time of 3.4 s is unfavorable for the aforementioned applications[11]. Achieving high responsivities and fast responses in photodetectors remains challenging.

In this context, the MoS_2/Ge material combination offers several intrinsic advantages for broadband and SWIR photodetection. Multilayer MoS_2 possesses a thickness-dependent bandgap (1.4–2.2 eV) with strong excitonic absorption in the visible and near-infrared region, while its indirect-bandgap nature in thicker flakes enables broadband absorption with suppressed dark current. Germanium, on the other hand, provides a narrow, indirect bandgap of 0.66 eV with high carrier mobility, long diffusion length, and strong absorption extending into the short-wave infrared. When vertically stacked, MoS_2 and Ge form a type-II band alignment that facilitates directional separation of photogenerated carriers and efficient tunneling-assisted injection under bias. This band alignment, combined with the defect-free interface achievable via van der Waals integration, allows fast carrier extraction without the slow trapping processes observed in conventional photomultiplication-based devices. Recent studies on MoS_2/Ge heterostructures have similarly demonstrated their potential for broadband and high-speed detection, further supporting the suitability of this material pairing for high-performance photodetectors.

Herein, we present a high-performance broadband photodetector exhibiting fast photocarrier multiplication by embedding a potential trap formed by a Ge homojunction and a mixed-dimensional van der Waals (vdW) heterojunction (MoS_2/Ge). The vdW heterojunctions of two-dimensional (2D) transition metal dichalcogenides (TMDCs) on conventional group IV or III–V semiconductors introduce more degrees of freedom to heterostructure band engineering because TMDCs can easily form heterojunctions via vdW forces regardless of the lattice constants[20–23]. The significant bandgap energy differences between TMDCs and semiconductor materials allow for creative band engineering to achieve broadband photodetectors[24], unlike previous attempts using bulk III–V heterojunctions. Moreover, double junctions consisting of vdW heterojunctions and homojunctions construct an engineered potential trap. While a prolonged stay of captured photocarriers in unintentionally present defect/interface trap results in an extremely slow response, the photocarriers in the engineered potential trap are instantly recombined upon removal of illumination, providing a high responsivity and a fast response time, simultaneously.

Results and discussion

Device scheme

In this study, we employed a MoS_2/Ge vdW heterojunction a Ge homojunction to achieve broadband and ultrafast photodetection. The vdW heterojunction between MoS_2 and Ge exhibited broadband photodetection owing to a significant bandgap energy difference (Eg_MoS_2: 1.4–2.2 eV[25]; Eg_Ge: 0.66 eV[26]. Moreover, in the n-Ge/p-Ge/MoS_2 double junction heterostructure, holes can be confined in the p-Ge region by tailoring the valence band. The accumulated photogenerated holes in the p-Ge lower the electron barrier between p-Ge and MoS_2, resulting in a photocurrent gain and a high responsivity[27,28]. The engineered hole confinement, in contrast to unintentional charge traps, exhibits a rapid diminishment of trapped holes upon the removal of light, thereby maintaining a fast response time.

A schematic illustration of the MoS_2/Ge double junction phototransistor is shown in Fig. 1a. The device is composed of a p-Ge/n-Ge homojunction and a p-Ge/n-MoS_2 heterojunction. The p-Ge shared by the two junctions is a base that serves as a hole confinement region. The n-MoS_2 and n-Ge functioned as an emitter and collector, respectively. A 100-nm-thick p-Ge was achieved via B-ion implantation on an n-Ge substrate, followed by fine etching in a dilute solution comprising NH_4OH and H_2O_2 (Figure S1 in Supporting Information). Prior to the transfer of the MoS_2 flake, the active area was defined by a circular opening with a diameter of 20 μm in an Al_2O_3 layer.

The details of the double junction phototransistor fabrication process and the optical image of the fabricated device are shown in Figure S2 (Supporting Information). The thickness of the transferred MoS_2 flakes was measured to be approximately 6.6 nm using atomic force microscopy (AFM), as shown in Fig. 1b. The AFM image shows that the MoS_2 flakes uniformly coated the exposed p-Ge region. Raman spectroscopic measurements were performed on the MoS_2/Ge vdW heterojunction. As shown in Fig. 1c, three Raman peaks appeared at 300.8, 383.8, and 408.8 cm^{-1}, which corresponded to the Ge–Ge phonon mode in Ge[29], as well as the E12g and A1g phonon modes in MoS_2 [30], respectively. These results indicate the pristine quality of MoS_2 in the junction region after transfer. The interface of MoS_2 and Ge was characterized by a transmission electron microscopy (TEM) as shown in Fig. 1d. A stack of multilayer MoS_2 was intact on the Ge, forming the heterojunction. Despite immediate transfer of MoS_2 after cleaning the Ge surface, a formation of a native oxide could not be avoided. Nonetheless, the very thin thickness of the native oxide, less than 2 nm, hardly affects carrier transport. The MoS_2 flake was transferred onto the Ge mesa using a dry viscoelastic stamp technique after defining the active region. Immediately before transfer, the exposed p-Ge surface was cleaned with a diluted HCl solution to suppress native oxide regrowth and to promote intimate van der Waals contact. During alignment and lamination, occasional issues such as microscopic interfacial bubbles or slight edge lifting were observed. These were mitigated by slowly releasing the polymer stamp and applying mild heating (60–80 °C) to enhance interfacial conformity, followed by a brief post-transfer anneal at 150 °C to stabilize adhesion. The quality of the resulting MoS_2/Ge interface was examined using TEM, Raman mapping, and KPFM (Fig. 1d and Fig. S3), all of which confirmed uniform contact without significant contamination or trapped residues.

The energy band diagram of Ge/MoS_2 double junction phototransistor was experimentally determined (see Fig. S3 and text in Supporting Information). To determine work functions the surface potentials of p-Ge, MoS_2, and the p-Ge/MoS_2 junction were 0.47, 0.19, and 0.2 eV, respectively, as measured using kelvin probe force microscopy (KPFM). The indiscernible potential difference between MoS_2 and p-Ge/MoS_2 could be attributable to the relatively thick MoS_2 (6 nm) in which the Ge underneath has little effect on the MoS_2 top surface. The bandgap energy of Ge was estimated using the Tauc plot to be 0.66 eV, which agrees with the value determined

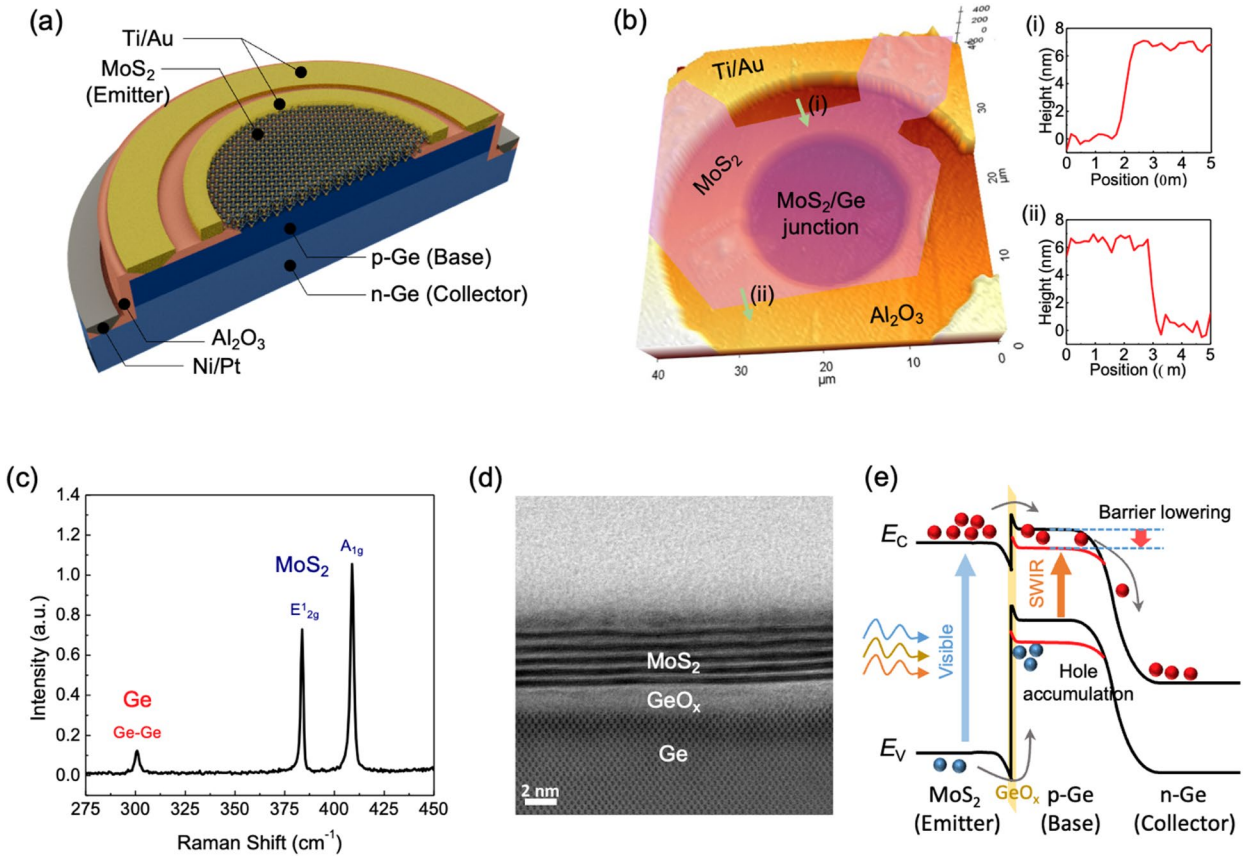

Fig. 1. Characterizations and operating principle of Ge/MoS_2 double junction phototransistor. (**a**) Schematic diagram of Ge/MoS_2 double junction phototransistor consisting of multilayer MoS2 flake, exposed p-Ge base region, and patterned metal contacts. (**b**) Atomic force microscopy image of Ge/MoS_2 heterojunction. Inset shows MoS_2 thickness corresponding to dashed green arrow, confirming a thickness of ~6.6 nm. (**c**) Raman spectra for Ge/MoS_2 vdW heterojunction. (**d**) Cross-sectional TEM image of the MoS_2/p-Ge interface, showing the vertically stacked multilayer MoS_2, native GeO_x layer, and underlying p-Ge. (**e**) Experimentally derived equilibrium band diagram of the Ge/MoS_2 double junction phototransistor constructed using KPFM-measured work functions, and schematic illustration of the device operation under illumination.

using electron energy loss spectroscopy (EELS)[18]. The bandgap energy of MoS_2 and electron affinities were derived from references[15,25,31]. At equilibrium, the energy band diagram of the MoS_2/p-Ge/n-Ge heterojunction reveals a staggered-gap (type II) at MoS_2/p-Ge. A conduction band offset and a valence band offset of 0.6 eV and 1.44 eV, respectively, were estimated.

The carrier transport and amplification mechanism in the device can be understood in terms of the resulting energy band diagram, as shown in Fig. 1e. The significant bandgap difference between Ge and MoS_2 contributed primarily to a high energy barrier to holes in the p-Ge instead of a conduction band offset in the heterojunction. Such dissimilar energy barriers in the heterojunction enabled MoS_2 to function as an ideal emitter, where more electrons from MoS_2 were transferred to p-Ge than holes from p-Ge to MoS_2[32]. The hole current injected via the p-Ge considered as a base would not propagate to MoS_2 (emitter); as such, electrons were induced from the emitter efficiently. The induced electrons were transported over the base and collected by the n-Ge, which is known as a collector. When the device functions as a photodetector, a positive bias is applied to the n-Ge with respect to the emitter (MoS_2), while the base (p-Ge) remains open. Hence, the base–emitter (p-Ge/n-MoS_2) is forward biased, whereas the base–collector (p-Ge/n-Ge) is reverse-biased. The potential of the base should be determined by equalizing the current across each heterojunction; therefore, the bias is primarily allocated to the reverse bias of the base–collector junction, as denoted by the black lines in the figure. When light is incident on n-MoS_2, visible light is primarily absorbed in the MoS_2 region, and SWIR light transparent to the MoS_2 is absorbed by Ge. Electrons and holes are photogenerated across the emitter–base heterojunction transport to the emitter and base, respectively. The electrons in the emitter flows out to the contact, but the holes are confined in the base. Hence, the accumulation of holes in the base lowers the energy barriers, particularly in the emitter–base heterojunction, thereby resulting in an injection of electrons from the emitter to the base, followed by a drift of electrons to the collector. As such, one photogenerated hole can induce more than one electron, enabling a high responsivity exceeding 100% external quantum efficiency (EQE).

Electrical characterization

Electrical measurements were performed on an n-MoS_2/p-Ge/n-Ge double junction phototransistor under dark conditions at room temperature. First, the p-Ge (base, B)/n-MoS_2 (emitter, E) heterojunction and p-Ge (B)/n-Ge (collector, C) homojunctions were separately characterized. Under a voltage swept from − 4 to 4 V, current rectifying behaviors were clearly observed at both p–n junctions, as shown in Fig. 2a. The ON/OFF current ratios (I_{ON}/I_{OFF}) of the B–E and B–C junctions were approximately 2.9×10^7 and 1.5×10^3, respectively. Saturation current in p-Ge/n-Ge homojunction was much higher than that in p-Ge/n-MoS_2 heterojunction because of germanium's narrow bandgap and a larger junction area of B-E junction (314 μm^2) compared to that of B-C junction (11,309 μm^2). The ideality factor (n) was estimated from the plot of ln(I) vs. V, and the values were 1.21 and 1.05 for the p-Ge/n-MoS_2 heterojunction and p-Ge/n-Ge junction, respectively. The slight deviations from the ideal diode can be ascribed to interface defects at the junction or additional series resistance[33,34].

Figure 2b shows the input characteristics (I_B–V_{BE}, where I_B and V_{BE} are the base current and base–emitter voltage, respectively) of the device with different V_{CB} biases. As observed in a forward-biased p–n junction, I_B increased exponentially with V_{BE}. As V_{CB} increased, I_B decreased and then rapidly saturated, implying that I_B is independent of the band shape above V_{CB} = 0.15 V because the reverse current of the base–collector junction had saturated. The output characteristics (I_C–V_{CE}, where I_C and V_{CE} are the collector current and collector–emitter voltage, respectively) in the common-emitter mode were measured at I_B at steps of 200 nA, as shown in Fig. 2c. It was observed that the input base current amplified under a V_{CE} of > ~ 3.5 V. At low V_{CE} values, it was insufficient to tunnel the native oxide of Ge and lower the potential barrier on the B–E junction owing to the difference in resistance between the B–E and B–C junctions. Hence, I_C increased exponentially after a sufficient V_{CE} was applied. Figure 2d shows the combined plot of I_B and I_C vs. V_{BE}, which is known as the Gummel plot. The common-emitter current gain (β), defined as I_C/I_B, is shown on the right axis in the figure. As V_{BE}

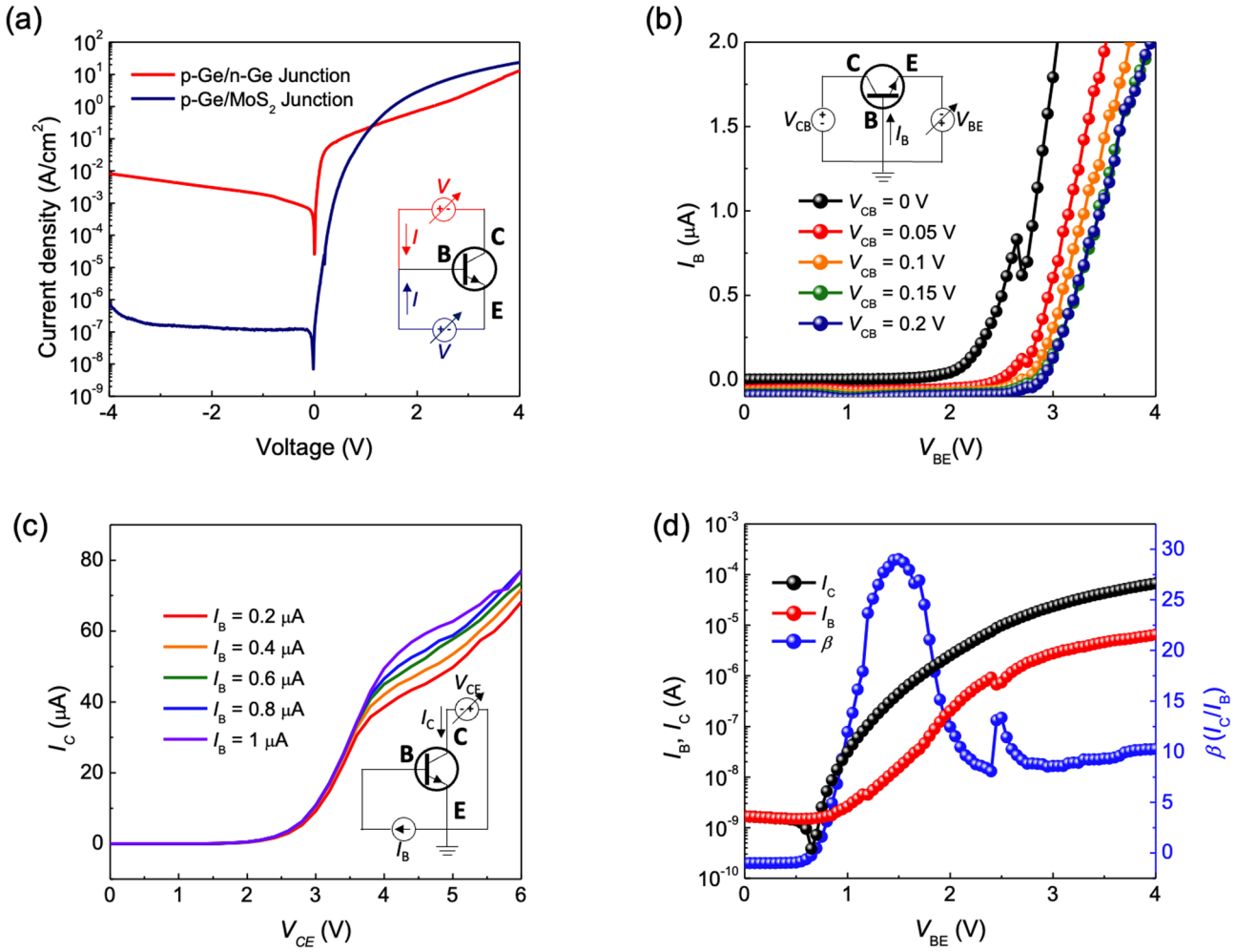

Fig. 2. Electrical characteristics of the fabricated device. (**a**) Current-density–voltage (J–V) characteristics of p-Ge/n-Ge (base-collector) homojunction and p-Ge/n-MoS_2 (emitter-base) heterojunction. Inset shows circuit schematics for measurements of p–n junctions. (**b**) Input characteristics for various V_{CE} and (**c**) output characteristics under different I_B of Ge/MoS_2 double junction transistors. Insets show circuit schematics for measurements of double juntion transistors. (**d**) Gummel plot of Ge/MoS_2 double junction transistor with corresponding current gain (β).

increased, both I_B and I_C increased exponentially in general. The β at $V_{BE} > 1$ V was distinct because the non-ideal recombination current at a low V_{BE} did not increase I_C. To the best of our knowledge, a maximum β value of approximately 29, which is the highest value recorded among 2D and three-dimensional (3D) vdW junction devices, has been reported. As V_{BE} increased further, the increase in I_C declined compared with that of I_B, and β diminished. This contributed to a high-level injection and series resistance, resulting in a simultaneous slope-over in both the I_B and I_C, as shown in the figure.

The electrical performance of the device was compared with those of previously reported hot electron transistors and heterojunction bipolar transistors based on 2D materials in terms of β and the collector current density (J_C). As shown in Figure S5, the n-MoS_2/p-Ge/n-Ge double junction phototransistor exhibited the highest J_C along with a decently high β. Devices such as photodetectors exploit these favorable performances, such as a high β to amplify photo-induced holes in the base region, which will be discussed below. Additionally, MoS_2/Ge double junction devices can be potentially deployed as electrical devices (e.g., switches and amplifiers).

Photoresponse characteristics

The photoresponse of the n-MoS_2/p-Ge/n-Ge double junction phototransistor was characterized by illuminating either a visible (466 nm) or SWIR (1550 nm) laser at room temperature. A positive V_{CE} was applied to the device with an open base, while maintaining the n-MoS_2 (E)/p-Ge (B) junction in forward bias and the p-Ge (B)/n-Ge (C) junction in reverse bias. Because the base is opened, the base current is governed by thermal generation in the dark and photogeneration in light. Figure 3a shows the I_C–V_{CE} curves under 466 and 1550 nm illumination under the same optical irradiance of 10 mW/cm^2 on a linear scale, and the inset shows the I_C–V_{CE} curves on a semi-logarithmic scale. An increase in I_C was observed for both the 466 and 1550 nm illuminations. Despite the lower photon energy of the 1550 nm light, which implies a higher number of incident photons at the same irradiance, the photoresponse of the 466 nm light was greater than that of the 1550 nm light. Because of the long penetration depth of 20 μm for the 1550 nm light in Ge[35], all the lights at 1550 nm were not absorbed in the p-Ge, whereas incident light was partially absorbed at the p-Ge/n-Ge junction.

Subsequently, the time-resolved photocurrent (I_{ph}) was characterized based on optical incident powers of 1, 3, 10, 30, 100, 300 and 1000 mW/cm^2 (Figure S6 in Supporting Information). The light modulated at a frequency of 1 kHz was illuminated on the device with a V_{CE} of 4 V. When the incident light power increased, the photocurrent increased linearly with a slope of 1.01 and 0.93 under 466 and 1550 nm illuminations, respectively, as shown in Figure S6b and d. This behavior verifies that trap-assisted conduction plays only a minimal role in our device, as no sublinear or trap-dominated scaling appears in the measured range. The photocurrent multiplication arises from engineered barrier modulation rather than trapping effects. For a more quantitative analysis of the response time, the transient photocurrent responses of the 466 and 1550 nm light were normalized, as shown in Fig. 3b. The response time (t_r) is defined as $t_r = (t_{rise} + t_{fall})/2$, where t_{rise} is the rising time when the light is "on," and t_{fall} is the falling time when the light is "off." For 466 nm laser modulation, the t_{rise} and t_{fall} were estimated to be 202.3 μs and 88.1 μs, respectively, giving rise to the tr of 145 μs. Under the illumination of the 1550 nm laser, a tr of 224 μs was obtained based on t_{rise} and t_{fall} of 214.9 and 232.8 μs, respectively. The extracted response times were limited by the maximum sampling rate of 110 μs, and the actual response speed was expected to be higher. Although the temporal resolution was limited by the sampling rate and prevented a more detailed analysis of the decay dynamics, the measured transient responses exhibit no slow tail or delayed relaxation behavior typically associated with deep trap states. This absence of long-lived relaxation components supports the proposed engineered potential-trap mechanism, in which carrier transport is dominated by rapid field-assisted collection rather than trap-mediated recombination. The fast rise and fall behaviors are therefore consistent with the expected response of the n-MoS_2/p-Ge/n-Ge double-junction structure.

The specific detectivity (D^*) is defined as $D^* = R \times (A \cdot BW)^{1/2}/i_n$, where R is the responsivity, A is the area, BW is the bandwidth, and i_n is the measured noise current. D^* can be estimated by assuming that the shot noise is dominant. The shot noise can be expressed as $i_n = (2 \cdot e \cdot I_d \cdot BW)^{1/2}$, where e is the electron charge, and I_d is the dark current. However, non-Ohmic contacts on the 2D materials and fluctuation of carrier transport over the vdW heterojunction may result in dominant noise components. For an accurate estimation of D^*, the noise power spectral density (NPSD) of the dark current was measured at various V_{CE} values, as shown in Figure S7 (Supporting Information). The NPSD curves for all biases indicated a 1/f dependence. A considerable increase in the spectral noise density as V_{CE} increased was observed. A frequency of 60 Hz and its harmonics were not the intrinsic noise of the device; instead, they originated from the 60 Hz power line. The noise currents with a BW of 1 kHz when V_{CE} were 1 and 4 V were 1.01×10^{-11} and 9.92×10^{-10} A/Hz$^{0.5}$, respectively. Figure 3c and d show the responsivity, EQE, and resulting D^* vs. V_{CE} for visible and SWIR lights, respectively (see calculation details in the Methods section). As V_{CE} increased, R and EQE increased linearly and reached maximum values of 7.6 A/W and 2,024%, respectively, for the 466 nm laser. Meanwhile, under the 1550 nm laser illumination, R and EQE increased at $V_{CE} > 0.5$ V owing to the potential barrier of the B–E junction and the absence of photogenerated carriers in MoS_2, reaching maximum values of 4.7 A/W and 376%, respectively. Despite the increase in responsivity at higher V_{CE} values at all detection ranges, the detectivity remained relatively constant because the noise current increased simultaneously. The maximum detectivities were 1.85×10^8 and 8.01×10^7 Jones under the 466 and 1550 nm illuminations, respectively. The detectivity was calculated by removing the input power noise (observed at intervals of 60 Hz, as shown in Figure S7). The detectivity was relatively low due to the high noise current caused by the high dark current. The specific detectivity of the device is primarily limited by the noise characteristics that originate from the mixed-dimensional MoS_2/Ge transport path. As shown in the noise spectral density measurements (Fig. S7), the device exhibits a combination of low-frequency 1/f noise attributed to interface states at the Ge mesa edge and multilayer MoS_2, as well as dark-current-induced noise at relatively high V_{CE}. These contributions increase the total noise current beyond the shot-noise limit, resulting in a realistic but moderate D^* value. This behavior is consistent with the mixed-dimensional geometry,

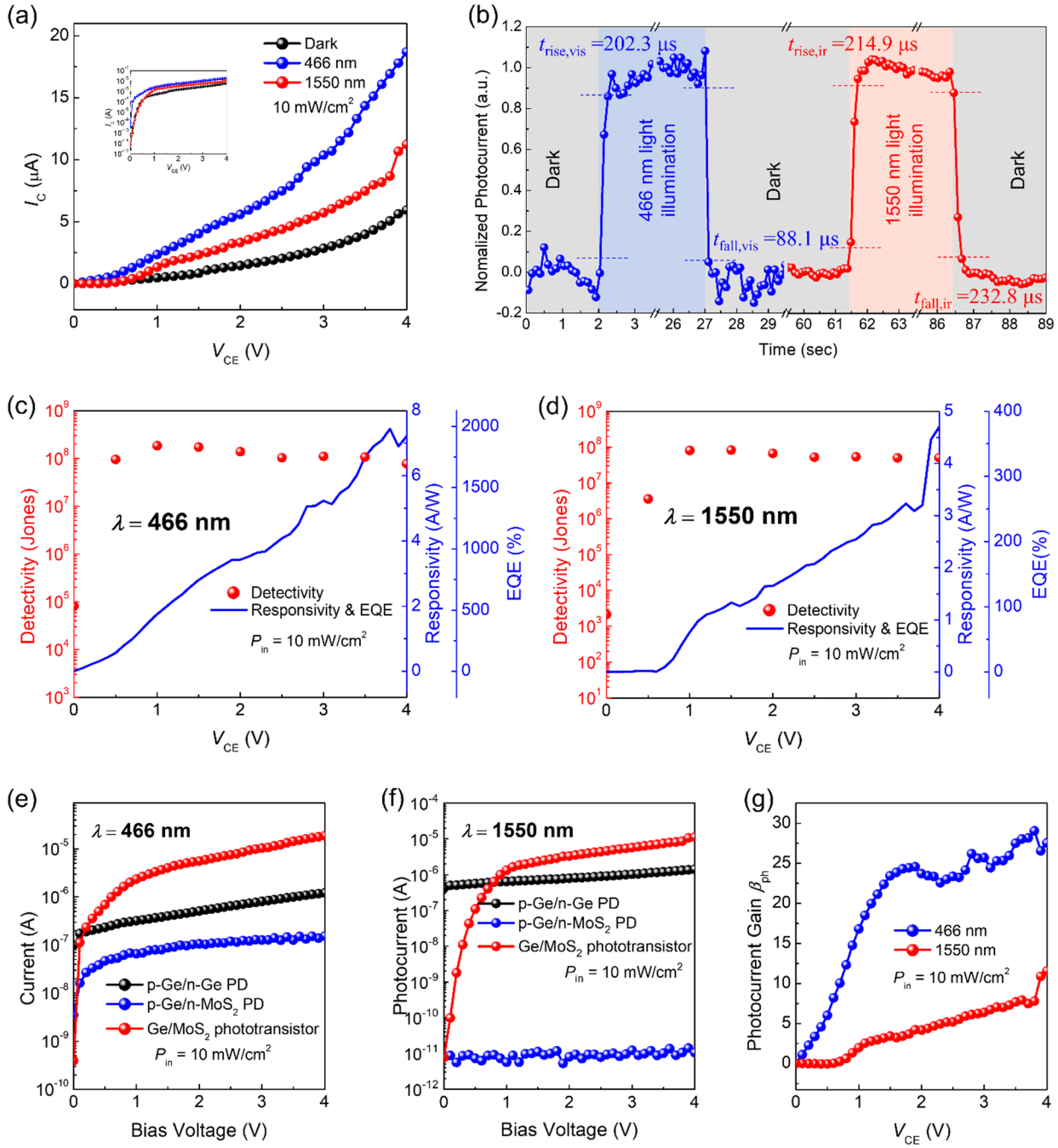

Fig. 3. Photoresponse characteristics of Ge/MoS_2 double junction phototransistor. (**a**) I_C–V_{CE} characteristics in dark condition and under 466 and 1550 nm illuminations of 10 mW/cm² on linear scale. Inset shows I_C–V_{CE} curves on semi-logarithmic scale. (**b**) Time-resolved photoresponse characteristics to pulsed 466 and 1550 nm lasers with frequency of 20 Hz. Insets show rising times and falling times under 466 and 1550 nm illuminations. Detectivity (D^*), responsivity (R), and external quantum efficiency (EQE) under (**c**) 466 nm and (**d**) 1550 nm illuminations of 10 mW/cm². Photocurrent vs. bias voltage of p-Ge/n-Ge homojunction, p-Ge/n-MoS_2 heterojunction, and Ge/MoS_2 double junction phototransistor under (**e**) 466 and (**f**) 1550 nm illumination of 10 mW/cm². (**g**) Photocurrent gain (β_{ph}) vs. V_{CE} for double junction phototransistor.

where the broad depletion region and high-field region in the p-Ge/n-Ge junction contribute to enhanced dark current and associated fluctuations. Further improvement may be achieved through Ge surface passivation, reduction of mesa-edge leakage, or optimized contact resistance, which can suppress both 1/f noise and high-bias noise components. Additionally, Figure S8 shows the spectral responsivity and external quantum efficiency of the Ge/MoS_2 double junction phototransistor, confirming its broadband detection capability from visible to SWIR wavelengths via photocurrent amplification.

Photocurrent multiplication in the n-MoS_2/p-Ge/n-Ge double junction phototransistor was directly evidenced by a comparison with the photoresponses of the p-Ge/n-MoS_2 heterojunction and p-Ge/n-Ge homojunction under 466 and 1550 nm illumination (Figs. 3e and f). Under the 466 nm illumination, the photocurrents (EQE) when the bias voltage was 4 V were 2.96×10^{-7} A (69.7%) and 1.54×10^{-7} A (36.2%) in the p-Ge/n-Ge homojunction and p-Ge/n-MoS_2 heterojunction, respectively, which indicate EQE values of less 100% (Fig. 3e). Meanwhile, the photocurrent (EQE) in the double junction phototransistor was 8.15×10^{-6} A (1,918.8%) at V_{CE} = 4 V, which implies that the photoresponse gain was present. The photocurrent gain (β_{ph}) of the double junction phototransistor, as calculated for 466 and 1550 nm illuminations, is shown in Fig. 3g. At higher bias voltages, β_{ph} reached the maximum measured values, i.e., 29.1 and 11.6 for 466 and 1550 nm, respectively, and these values were similar to the base current gain obtained in the aforementioned electrical characterization.

For photodetectors and image sensors, responsivity and response speed are critical figures-of-merit. To detect weak light in an image sensor, the photodetector must have both a fast response time and a high responsivity. Figure 4 shows the cut-off frequencies and responsivities of several previously reported broadband photodetectors. Without photocurrent gain, devices exhibit a rapid response time because carriers are photogenerated and then promptly vanish in response to the on/off of light[14,15,17]. On the other hand, in the devices with a high responsivity due to photocurrent gain, photogenerated carriers do not completely disappear when the light is switched off, resulting in a long response time[11–13]. In other words, it has been challenging to develop desirable features in both. It is worth noting that our phototransistor outperformed other photodetectors in terms of response time and responsivity. This capability is credited with broadband imaging, including SWIR for night vision and harsh environments in self-driving. To place our device performance in a broader context, Fig. 4 provides a quantitative comparison with recently reported broadband photodetectors, including graphene-QD

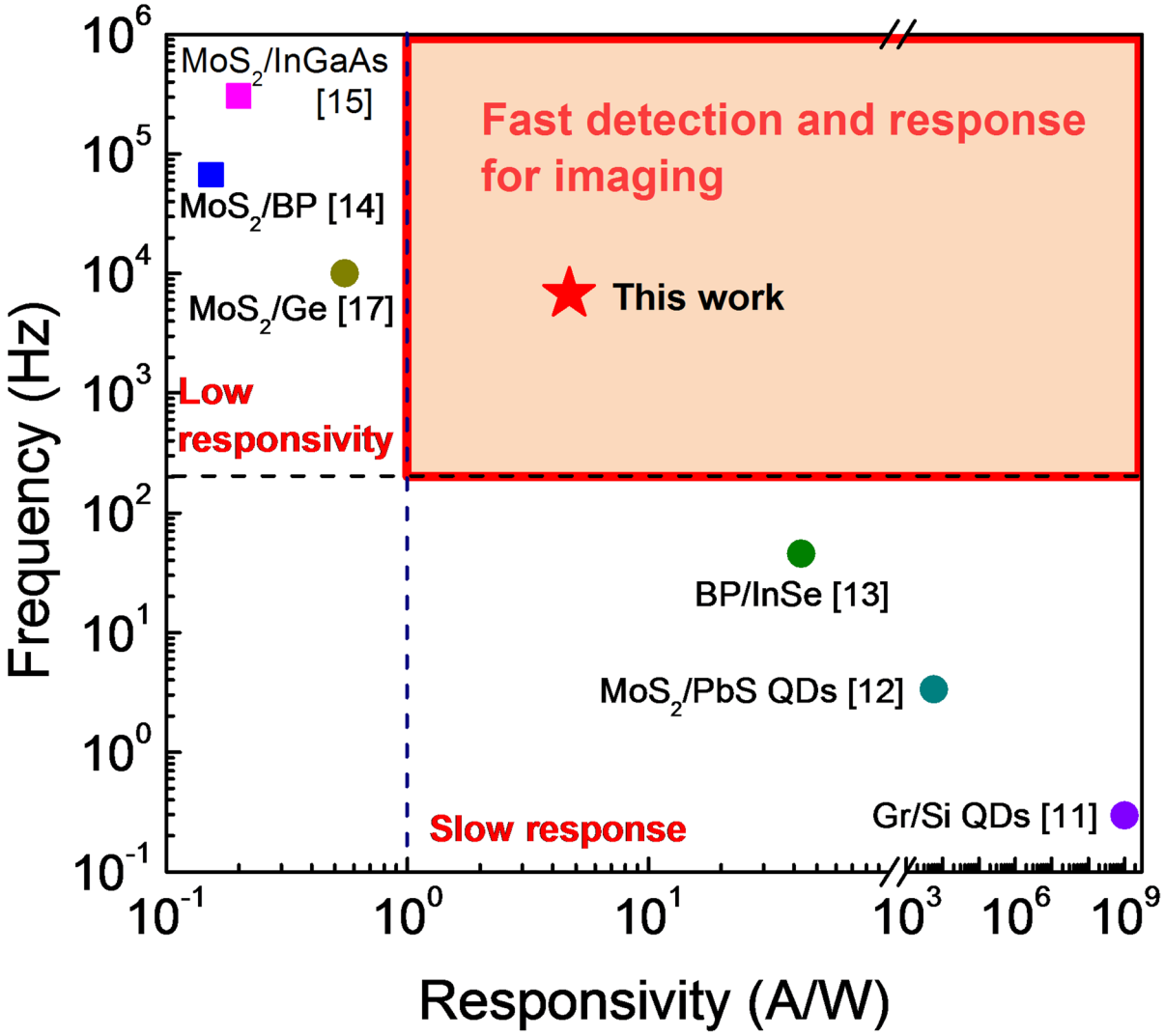

Fig. 4. Comparison of frequency vs. responsivity of Ge/MoS_2 double junction phototransistor and several photodetectors for broadband detection. Dashed horizontal line indicates frequency of 200 Hz, and dashed vertical line indicates 100% EQE (1.24 A/W for 1,550 nm light).

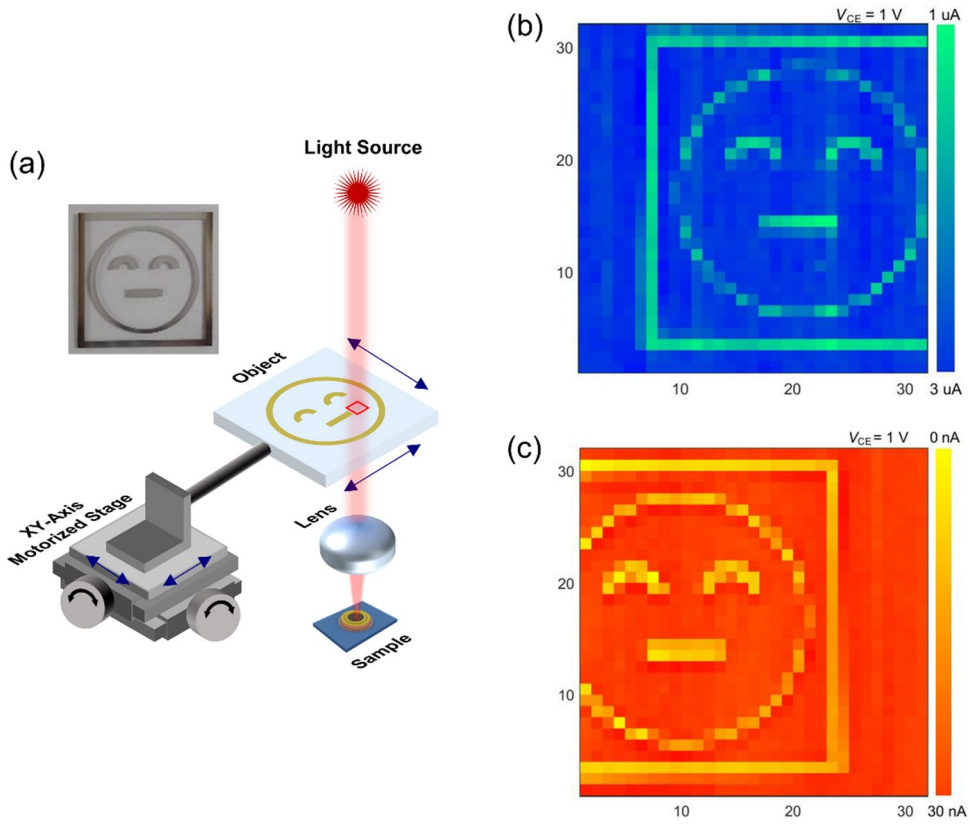

Fig. 5. (**a**) Schematic diagram of measurement systems used for broadband imaging. A smile-patterned aluminum mask is illuminated by either 466-nm or 1550-nm laser, and the transmitted light is focused (50-mm lens) onto the device. Inset shows the mask pattern fabricated on quartz. A 32 × 32 pixel grid is acquired using a 20-μm step size on a motorized XY stage under (**b**) 466 and (**c**) 1550 nm illuminations.

hybrids, TMDC-III-V heterojunctions, and mixed-dimensional van der Waals devices. Many high-responsivity devices rely on deep trap–mediated photomultiplication, achieving responsivities above 10^2–10^3 A/W but suffering from millisecond-to-second response times. Conversely, high-speed devices often exhibit response times below 1 ms but with limited responsivity due to the absence of internal gain. In contrast, our MoS_2/Ge double-junction phototransistor simultaneously achieves sub-millisecond response (145 s at 466 nm) and high responsivity (7.6 A/W), placing it in a distinct performance regime that bridges the long-standing tradeoff between speed and gain. This balanced performance directly reflects our engineered potential-trap design, where carrier confinement in the p-Ge base enhances photocurrent without invoking slow trap dynamics. As such, the device uniquely positions itself among state-of-the-art broadband detectors by offering both high sensitivity and fast temporal response, enabling practical imaging across visible and SWIR wavelengths.

Additionally, the broadband imaging capability of our device was investigated. Figure 5a shows a schematic diagram of the measurement systems used for broadband imaging. A smile image, which was mounted onto the XY-axis motorized stage, was placed between the light source and lens. The light incident from the 466 and 1550 nm lasers was focused onto the phototransistor via the lens after it passed through the object. Visible/SWIR smile images of 32 × 32 pixels are clearly depicted in Figs. 5b–c. These results imply that the device proposed herein can be utilized as a broadband imaging sensor from the visible to SWIR light range.

Conclusions

In this study, we demonstrate a MoS_2/Ge double junction phototransistor and investigated its electrical and photoresponse characteristics. The electrical properties obtained demonstrated their potential as an electronic device and a photodetector with β = 29. The MoS_2/Ge phototransistor allowed broadband detection from the visible to SWIR wavelength range. The double junction phototransistor exhibited high photocurrent amplification, with β_{ph} = 29.1 (11.6) at 466 (1550) nm. Moreover, the fabricated phototransistor exhibited a high responsivity of 7.4 (4.7) A/W and fast t_{rise} (t_{fall}) of 202.3 (214.9) and 88.1 (232.8) μs, respectively, under a 466 (1550) nm illumination. The fast broadband photodetection demonstrated in this study, which was achieved by utilizing a heterogeneously integrated Ge/TMDC structure, will greatly facilitate bringing improved photodetectors to the market, such as an eye safe detector operating in the 1550 nm wavelength as opposed to the harmful 940 nm wavelength, or sensors that allow to obtain clear visibility in adverse weather conditions. The concept of a vdW Ge/TMDC heterojunction addition to conventional homojunction device can be adopted to

improve the performance of many conventional III–V devices that operate with inferior fundamental operations that limit their performances with much cheaper cost. The 2D/3D heterostructure concept demonstrated here removes this bottleneck, thereby providing opportunities for the development of ultrahigh-performance electric and optoelectronic devices.

Methods

Material characterization

Morphology was measured using AFM (XE100, Park Systems) in non-contact mode. Kelvin probe force microscopy measurement was performed using AFM (XN-10, Park Systems) in non-contact mode. Micro-Raman spectroscopy measurements (LabRam HR Evolution, Horiba) of the Ge/MoS_2 double junction phototransistor were performed based on a spatial resolution of 1 μm and a 532 nm excitation laser under ambient conditions. The sample for TEM analysis was prepared using a focused ion beam system (Quanta 3D FEG, FEI). TEM was performed using a high-resolution TEM (JEM-2100 F, JEOL) with an operating voltage of 200 kV.

Electrical and optoelectrical measurements

Electrical and optoelectrical characteristic measurements were performed using a semiconductor parameter analyzer (4200 A-SCS, Keithley Instruments) with 466 and 1550 nm diode pumped solid-state lasers (Civil laser). The transient characteristics were measured using a source meter (2614 B, Keithley Instruments) with pulsed 466 and 1550 nm lasers. The spectral responsivities were measured using monochomater (MonoRa200, Dongwoo Optron) with Xenon lamp. The NPSDs were measured at a sampling rate of 1,600 Hz under dark conditions using a dynamic signal analyzer (35670 A, Agilent).

Response speed, responsivity, detectivity, and photocurrent gain extraction

The t_{rise} and t_{fall} were defined as the time intervals that increased from 10% to 90% at the peak values and decreased from 90% to 10%, respectively.

To extract the responsivity, the photocurrent was calculated as $I_{ph} = I_{light} - I_{dark}$, where I_{light} is the measured current with illuminations of various power intensities and wavelengths, and I_{dark} is the measured current under dark conditions. The responsivity was calculated as $R = I_{ph}/P_{in}$, where I_{ph} and P_{in} are the photocurrent and incident optical power, respectively.

To characterize in, the measured current NPSD was square-rooted and integrated by the *BW*, where *BW* is the specified bandwidth. The noise equivalent power (NEP) of our device was calculated as NEP = i_n/R, where in is the total noise current in units of $A{\cdot}Hz^{-0.5}$. The detectivity is expressed as $D^* = A^{-0.5}/\mathrm{NEP}$, where *A* is the area of the heterojunction phototransistor.

The photocurrent gain was extracted as $\beta_{ph} = I_{ph,\,tr}/I_{ph,\,pn}$, where $I_{ph,\,tr}$ is the photocurrent of the vdW Ge/MoS_2 heterojunction phototransistor, and $I_{ph,\,pn}$ is the photocurrent of the p–n junctions.

Broadband imaging measurements

The broadband imaging capability of the Ge/MoS_2 double-junction phototransistor was characterized using a raster-scanning optical setup designed to acquire two-dimensional transmitted images under both visible (466 nm) and short-wave infrared (1550 nm) illumination. As shown in Fig. 5a, a patterned object (smile image) mounted on a computer-controlled XY motorized stage (Zaber Technologies) was positioned between the monochromatic light source and an achromatic focusing lens. The 466 nm and 1550 nm diode-pumped solid-state lasers (CivilLaser) were first expanded and collimated and then directed toward the target object. The transmitted light passing through the patterned aperture was subsequently focused onto the active area of the phototransistor using a 50-mm focal-length plano-convex lens. Based on the optical configuration, the diameter of the focused spot at the device plane was approximately 10–12 μm, comparable to the lateral dimension of the base–emitter junction region.

During imaging, the XY stage was programmed to scan a 32 × 32 grid with a step size of 20 μm, ensuring complete sampling across the patterned region. At each pixel position, the device was operated in the phototransistor configuration by applying a collector–emitter voltage of V_{CE} = 4 V while keeping the base terminal electrically floating. The photocurrent at each coordinate was measured using a semiconductor parameter analyzer (4200 A-SCS, Keithley Instruments). A measurement integration time of 10 ms was used for each pixel, providing sufficient signal averaging without degrading the total image acquisition time. The photocurrent signal at each position was converted into a pixel intensity value, and the complete 2D image was reconstructed by mapping the measured photocurrent values to their corresponding spatial coordinates.

Data availability

The datasets used and/or analysed during the current study available from the corresponding author on reasonable request.

Received: 10 August 2025; Accepted: 2 January 2026
Published online: 08 January 2026

References

1. Naboulsi, M. A. Fog Attenuation prediction for optical and infrared waves. *Opt. Eng.* **43**(2), 319. https://doi.org/10.1117/1.1637611 (2004).
2. Driggers, R. G., Hodgkin, V. & Vollmerhausen, R. What good is SWIR? Passive day comparison of VIS, NIR, and SWIR. *Infrared Imaging Syst. Des. Anal. Model. Test. XXIV*. **8706**, 87060L. https://doi.org/10.1117/12.2016467 (2013).

3. Martin, T., Brubaker, R., Dixon, P., Gagliardi, M. A. & Sudol, T. 640x512 InGaAs focal plane array camera for visible and SWIR imaging. *Infrared Technol. Appl. XXXI*. **5783**, 12. https://doi.org/10.1117/12.603406 (2005).
4. Malchow, D., Battaglia, J., Brubaker, R. & Ettenberg, M. High speed short wave infrared (SWIR) imaging and range gating cameras, in *Thermosense XXIX*, Vol. 6541, 654106. https://doi.org/10.1117/12.721747 (2007).
5. Bernini, N., Bertozzi, M., Cerri, P. & Fedriga, R. I. SWIR cameras for the automotive field: two test cases. *ISRN Automot. Eng.* **2014**, 1–11. https://doi.org/10.1155/2014/858979 (2014).
6. Tsuboi, S. & Jin, T. Shortwave-infrared (SWIR) fluorescence molecular imaging using indocyanine green-antibody conjugates for the optical diagnostics of cancerous tumours. *RSC Adv.* **10**(47), 28171–28179. https://doi.org/10.1039/d0ra04710d (2020).
7. Qi, J. et al. Real-Time and high-resolution bioimaging with bright aggregation-induced emission dots in short-wave infrared region. *Adv. Mater.* **30**(12), 1706856. https://doi.org/10.1002/adma.201706856 (2018).
8. Yu, Z. et al. High-Resolution shortwave infrared imaging of vascular disorders using gold nanoclusters. *ACS Nano*. **14**(4), 4973–4981. https://doi.org/10.1021/acsnano.0c01174 (2020).
9. Narang, N. & Bourlai, T. Face recognition in the SWIR band when using single sensor multi-wavelength imaging systems. *Image Vis. Comput.* **33**, 26–43. https://doi.org/10.1016/j.imavis.2014.10.005 (2015).
10. Goossens, S. et al. Broadband image sensor array based on graphene-CMOS integration. *Nat. Photonics*. **11**(6), 366–371. https://doi.org/10.1038/nphoton.2017.75 (2017).
11. Ni, Z. et al. Plasmonic silicon quantum Dots enabled High-Sensitivity ultrabroadband photodetection of Graphene-Based hybrid phototransistors. *ACS Nano*. **11**(10), 9854–9862. https://doi.org/10.1021/acsnano.7b03569 (2017).
12. Kufer, D. et al. Hybrid 2D-0D MoS2-PbS quantum Dot photodetectors. *Adv. Mater.* **27**(1), 176–180. https://doi.org/10.1002/adma.201402471 (2015).
13. Cao, R. et al. Black Phosphorous/Indium Selenide photoconductive detector for visible and Near-Infrared light with high sensitivity. *Adv. Opt. Mater.* **7**(12), 1–7. https://doi.org/10.1002/adom.201900020 (2019).
14. Ye, L., Li, H., Chen, Z. & Xu, J. Near-Infrared photodetector based on MoS2/Black phosphorus heterojunction. *ACS Photonics*. **3**(4), 692–699. https://doi.org/10.1021/acsphotonics.6b00079 (2016).
15. Geum, D. M. et al. Arrayed MoS2–In0.53Ga0.47As Van der Waals heterostructure for High-Speed and broadband detection from visible to Shortwave-Infrared light. *Small* https://doi.org/10.1002/smll.202007357 (2021).
16. Heves, E. & Gurbuz, Y. Highly responsive, solution-based Al/PbS and Au-Ti/PbS Schottky photodiodes for SWIR detection. *IEEE Sens. J.* **14**(3), 816–820 (2014).
17. Kim, S. G. et al. Infrared detectable MoS2 phototransistor and its application to artificial multilevel Optic-Neural synapse. *ACS Nano*. **13**(9), 10294–10300. https://doi.org/10.1021/acsnano.9b03683 (2019).
18. Hwang, A. et al. Visible and infrared dual-band imaging via Ge/MoS2van der Waals heterostructure. *Sci. Adv.* **7**(51), 1–9. https://doi.org/10.1126/sciadv.abj2521 (2021).
19. Lee, C. H. et al. Design of p-WSe 2 /n-Ge heterojunctions for High-Speed broadband photodetectors. *Adv. Funct. Mater.* **2107992**, 2107992. https://doi.org/10.1002/adfm.202107992 (2021).
20. Choi, W. et al. Recent development of two-dimensional transition metal dichalcogenides and their applications. *Mater. Today*. **20**(3), 116–130. https://doi.org/10.1016/j.mattod.2016.10.002 (2017).
21. Lopez-Sanchez, O. et al. Light generation and harvesting in a Van der Waals heterostructure. *ACS Nano*. **8**(3), 3042–3048. https://doi.org/10.1021/nn500480u (2014).
22. Vashishtha, P. et al. Epitaxial interface-driven photoresponse enhancement in monolayer WS2-MoS2 lateral heterostructures. Adv. Funct. Mater., Early View. https://doi.org/10.1002/adfm.202512962 (2025)
23. Vashishtha, P. et al. Self-powered broadband photodetection of MoS2/Sb2Se3 heterostructure. *ACS Appl. Opt. Mater.* **1**, 1952. https://doi.org/10.1021/acsaom.3c00300 (2023).
24. Park, Y., Hwang, A. J., Lee, C., Yoo, G. & Heo, J. Broadband photodetection of MoS2/p-Ge/n-Ge bipolar heterojunction phototransistor. in *Conference on Lasers and Electro-Optics, CLEO 2021 - Proceedings* STh5B.3 (2021). https://doi.org/10.1364/cleo_si.2021.sth5b.3.
25. Zhao, Z. Y. & Liu, Q. L. Study of the layer-dependent properties of MoS2 nanosheets with different crystal structures by DFT calculations. *Catal. Sci. Technol.* **8**(7), 1867–1879. https://doi.org/10.1039/c7cy02252b (2018).
26. Trommer, J. et al. Enabling energy efficiency and Polarity control in germanium nanowire transistors by individually gated nanojunctions. *ACS Nano*. **11**(2), 1704–1711. https://doi.org/10.1021/acsnano.6b07531 (2017).
27. Su, B. W. et al. A gate-tunable symmetric bipolar junction transistor fabricated: Via femtosecond laser processing. *Nanoscale Adv.* **2**(4), 1733–1740 (2020). https://doi.org/10.1039/d0na00201a
28. Li, H., Ye, L. & Xu, J. High-Performance broadband Floating-Base bipolar phototransistor based on WSe2/BP/MoS2 heterostructure. *ACS Photonics*. **4**(4), 823–829. https://doi.org/10.1021/acsphotonics.6b00778 (2017).
29. Prucnal, S. et al. Superconductivity in single-crystalline aluminum- and gallium-hyperdoped germanium. *Phys. Rev. Mater.* **3**(5), 1–10. https://doi.org/10.1103/PhysRevMaterials.3.054802 (2019).
30. Lee, C. et al. Anomalous lattice vibrations of single- and few-layer MoS2. *ACS Nano*. **4**(5), 2695–2700. https://doi.org/10.1021/nn1003937 (2010).
31. Nishimura, T., Luo, X., Matsumoto, S., Yajima, T. & Toriumi, A. Almost pinning-free bismuth/Ge and /Si interfaces. *AIP Adv.* **9**(9), 095013 https://doi.org/10.1063/1.5115535 (2019).
32. Anderson, B. & Anderson, R. *Fundamentals of Semiconductor Devices*1st edn (McGraw-Hill College, 2004).
33. Choudhary, N. et al. Two-dimensional lateral heterojunction through bandgap engineering of MoS_2 via oxygen plasma. *J. Phys. Condens. Matter*. **28**(36), 364002 https://doi.org/10.1088/0953-8984/28/36/364002 (2016).
34. Yan, X. et al. High performance amplifier element realization via MoS2/GaTe heterostructures. *Adv. Sci.* **5**(4), 1–7. https://doi.org/10.1002/advs.201700830 (2018).
35. Eng, P. C., Song, S. & Ping, B. State-of-the-art photodetectors for optoelectronic integration at telecommunication wavelength. *Nanophotonics* **4**(1), 277–302 https://doi.org/10.1515/nanoph-2015-0012 (2015).

Author contributions

Y.P. fabricated the devices and performed the electrical and optical measurements. H.B.J and H.Y.J performed the material characterizations. Y.P., M.J., S.S., G.Y., and J.H. analyzed the experiments and wrote the manuscript. All authors contributed to the discussion and analysis of the results of the manuscript. J.H. supervised the project.

Funding

This study was supported by the National R&D Program through the National Research Foundation of Korea (NRF) funded by the Ministry of Science and ICT (RS-2024-00438811, RS-2025-00564261, RS-2025-02217113).

Declarations

Competing interests
The authors declare no competing interests.

Additional information
Supplementary Information The online version contains supplementary material available at https://doi.org/10.1038/s41598-026-35134-z.

Correspondence and requests for materials should be addressed to J.H.

Reprints and permissions information is available at www.nature.com/reprints.

Publisher's note Springer Nature remains neutral with regard to jurisdictional claims in published maps and institutional affiliations.